


ARTICLE

DOI: 10.1038/s41467-017-00646-w

OPEN

Novel ecto-tagged integrins reveal their trafficking in live cells

Clotilde Huet-Calderwood¹, Felix Rivera-Molina², Daniel V. Iwamoto¹, Emil B. Kromann^{2,3}, Derek Toomre² & David A. Calderwood ^{1,2}

Integrins are abundant heterodimeric cell-surface adhesion receptors essential in multicellular organisms. Integrin function is dynamically modulated by endo-exocytic trafficking, however, major mysteries remain about where, when, and how this occurs in living cells. To address this, here we report the generation of functional recombinant $\beta 1$ integrins with traceable tags inserted in an extracellular loop. We demonstrate that these 'ecto-tagged' integrins are cell-surface expressed, localize to adhesions, exhibit normal integrin activation, and restore adhesion in $\beta 1$ integrin knockout fibroblasts. Importantly, $\beta 1$ integrins containing an extracellular pH-sensitive pHluorin tag allow direct visualization of integrin exocytosis in live cells and revealed targeted delivery of integrin vesicles to focal adhesions. Further, using $\beta 1$ integrins containing a HaloTag in combination with membrane-permeant and -impermeant Halo dyes allows imaging of integrin endocytosis and recycling. Thus, ecto-tagged integrins provide novel powerful tools to characterize integrin function and trafficking.

¹Department of Pharmacology, Yale University School of Medicine, 333 Cedar Street, New Haven, Connecticut 06520, USA. ²Department of Cell Biology, Yale University School of Medicine, 333 Cedar Street, New Haven, Connecticut 06520, USA. ³Department of Biomedical Engineering, Yale University, 333 Cedar Street, New Haven, Connecticut 06520, USA. Clotilde Huet-Calderwood and Felix Rivera-Molina contributed equally to this work. Correspondence and requests for materials should be addressed to D.T. (email: derek.toomre@yale.edu) or to D.A.C. (email: david.calderwood@yale.edu)

The ability of cells to sense and adhere to the surrounding extracellular matrix (ECM) is essential for multicellular life. Integrins, a family of heterodimeric $\alpha\beta$ adhesion receptors, enable this by binding specific ECM ligands with their ectodomains and associating with a wide range of cytoskeletal and signaling proteins through their cytoplasmic tails, permitting bidirectional transmembrane communication that is essential for cell adhesion, migration, differentiation, and survival^{1–3}. Integrin-mediated adhesion and signaling is regulated by diverse factors including conformational rearrangements that alter the affinities of integrins for their extracellular ligands, clustering of integrins and their intracellular binding partners into cytoskeletal-associated adhesions, as well as the dynamic endocytosis, sorting, and exocytosis of integrins themselves^{1, 2, 4, 5}.

Although much is known about integrins at the atomic level (i.e., the molecular basis for ligand binding and the conformational

domain rearrangements involved in integrin activation^{6–9}), fundamental insight into the spatial and temporal control of integrin functions at the cellular level is critically lacking. Specifically, where and when integrins become engaged/disengaged to enable physiological responses such as adhesion, migration, differentiation, and survival, and how spatial and temporal dysregulation of these processes contributes to disease, remain to be fully elucidated. Integrin trafficking, as a way to control integrin surface levels via exocytosis, endocytosis, and recycling, has received considerable interest^{4, 5, 10}, especially as alterations in integrin trafficking have been shown to promote invasion and cancer metastasis^{4, 11–13}. Many molecular adapters involved in membrane trafficking have been found to regulate integrin surface levels and to affect integrin-mediated activities, with some adapters shown to directly bind integrin subunits^{4, 5, 10, 14, 15}. Although biochemical assays such as cell-surface biotinylation or integrin labeling with ligand or

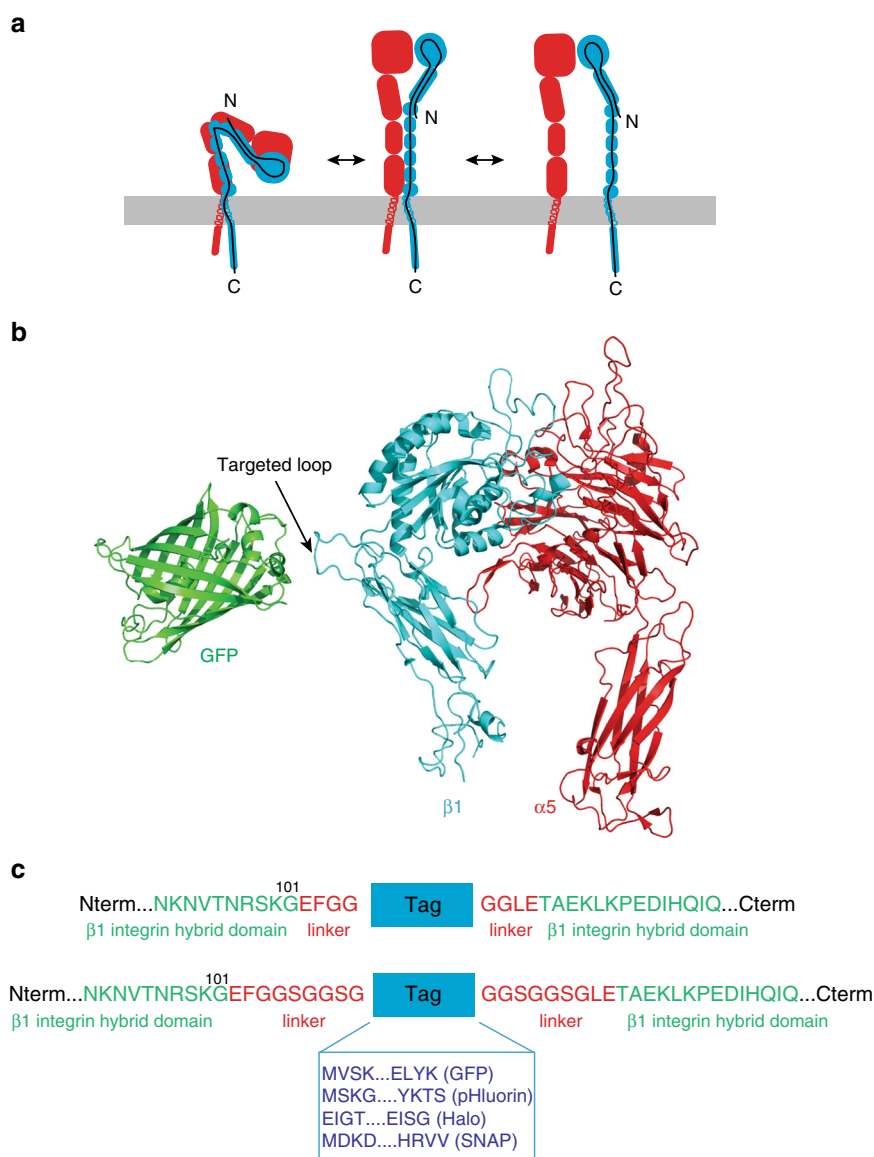


Fig. 1 Design of an ecto-tagged $\beta 1$ integrin. **a** Cartoon of the conformational changes in the integrin heterodimer during integrin activation; α subunit is depicted in red, β subunit in blue, and the black line represents the β subunit polypeptide chain. **b** Ribbon diagram of the crystal structures of the $\alpha 5\beta 1$ integrin head piece (PDB: 3VI4) and GFP (PDB: 1GFL). The hybrid domain loop into which ecto-tags were inserted is indicated. **c** Zoom-in on the amino acid sequence of human ecto-tagged $\beta 1$ integrins at the tag insertion site. Each ecto-tag (GFP, pHluorin, Halo, and SNAP, in blue, N- and C-terminal sequences specified) was inserted into the hybrid domain of human $\beta 1$ integrin between residues Gly101 and Tyr102 (in green). Linkers of 4 or 9 amino acids (in red) were added on each side of the tag to facilitate cloning and provide flexibility

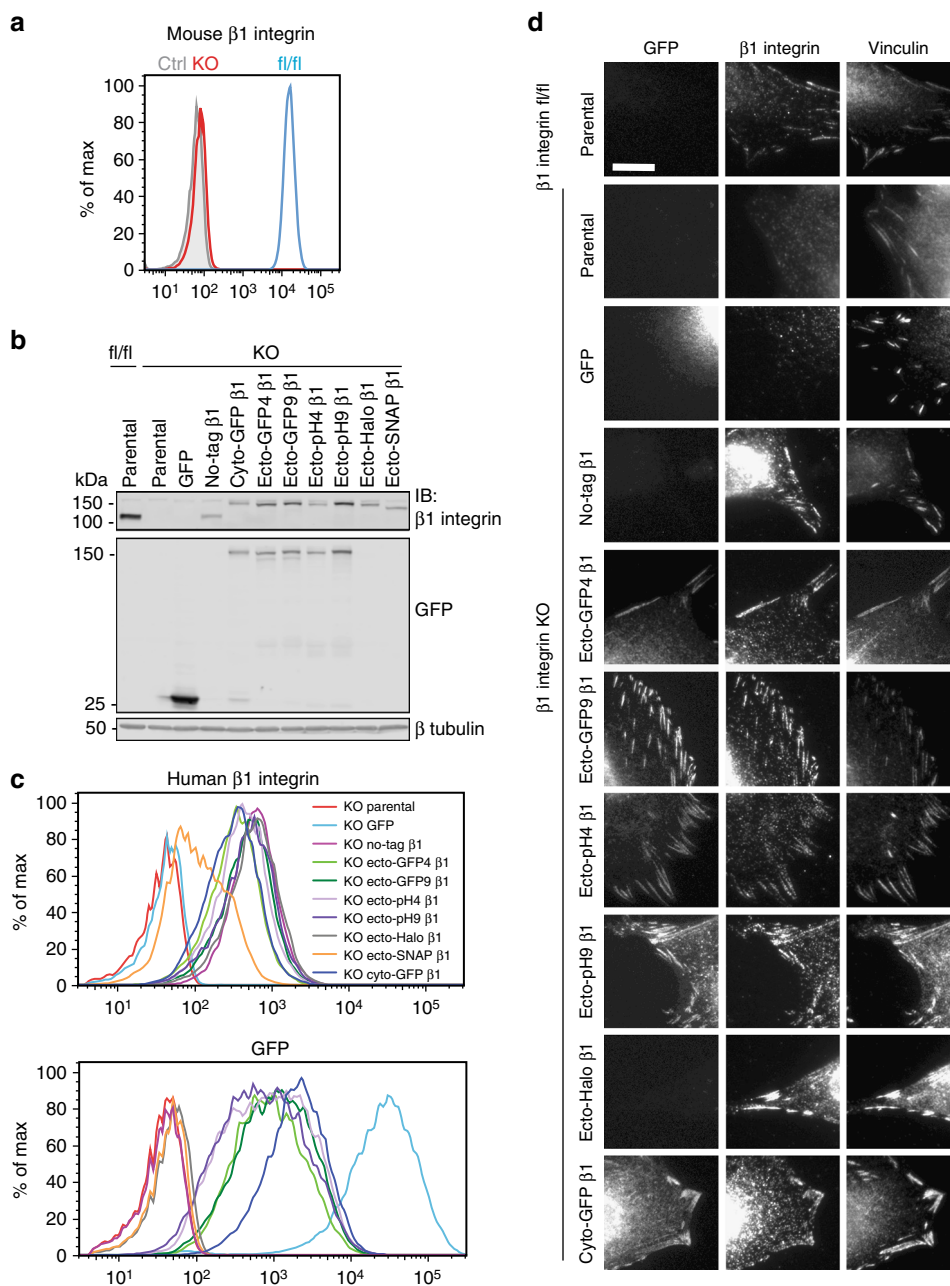


Fig. 2 Ecto-tagged $\beta 1$ integrins translocate to the cell surface and target to FAs. **a** Flow cytometric analysis of cell surface levels of mouse $\beta 1$ integrin in $\beta 1$ integrin *fl/fl* (blue peak) and KO fibroblasts (red peak), and control unstained KO fibroblasts (gray peak). **b** Immunoblot detection of endogenous and ectopic $\beta 1$ integrins in lysates of 100,000 *fl/fl* and KO fibroblasts using a pan- $\beta 1$ integrin antibody (top panel) and an anti-GFP antibody (middle panel). Tubulin was used as a loading control (bottom panel). Uncropped blots are available in Supplementary Fig. 10. **c** Flow cytometric analysis of cell surface levels of human $\beta 1$ integrins (top panel) and GFP fluorescence (bottom panel) in parental and reconstituted $\beta 1$ integrin KO fibroblasts. **d** Microscopy images of parental and reconstituted *fl/fl* and KO fibroblasts showing GFP epifluorescence (left column), $\beta 1$ integrin immunofluorescence with 9EG7 antibody (center column), and vinculin immunofluorescence (right column). Scale bar, 10 μ m

antibodies have allowed measurement of integrin internalization and recycling rates, fully understanding how integrin trafficking is orchestrated and its role in cell physiology and pathology requires sophisticated microscopy tools designed to follow specific pools of integrins in live cells. To date, direct visualization of integrin exocytosis has not been possible but integrin endocytosis has been imaged using either integrin subunits fused to a cytoplasmic fluorescent protein (cyto-tagged), or indirect integrin labeling with specific ligands or antibodies^{15–17}. Together with FRAP and photoconversion techniques, cyto-tagged integrins have been powerful tools to visualize integrin internalization and turnover^{18, 19}.

Photoactivation in Total Internal Reflection Fluorescence Microscopy (TIRFM) has been used to localize the sites of integrin internalization¹⁸ and to determine to which portion of the cell $\alpha 5\beta 1$ is preferentially delivered¹¹. However, cyto-tagged integrins have a number of shortcomings. First, the inaccessibility of a cytoplasmic tag to the extracellular compartment precludes the use of affinity or enzymatic tags for selective and covalent surface labeling. Second, the insensitivity of a cytoplasmic tag moiety to the extracellular environment prevents the use of pH-sensitive fluorophores to discriminate whether the integrins are at the cell surface or in endomembranes. Third, there are valid concerns

about the impact of the cytoplasmic tag on the binding of the numerous cytoplasmic partners^{19–22} to the relatively short (20–70 amino acids) cytoplasmic tail of integrin subunits.

As a consequence, we set out to design functional recombinant $\beta 1$ integrins containing an accessible and traceable extracellular tag (ecto-tag). The main challenge was to identify, within the multi-domain structure of the $\beta 1$ integrin ectodomain, a suitable tag insertion site that would affect neither the overall folding of each subdomain, nor heterodimerization with the α integrin subunit, nor the ligand-binding activity and specificity. Moreover, because it is generally thought that integrin activation and ligand binding trigger substantial structural rearrangements, including extension of the integrin from a bent to extended conformation and reorientation of specific domains within the complex^{3, 6, 23}, the ecto-tag should not impact the equilibrium between active and inactive conformations so as to preserve integrin function.

Here we report the successful generation of functional ecto-tagged $\beta 1$ integrins with various genetic and chemical-genetic fluorescent tags (GFP, pHluorin, or Halo tags) inserted into an exposed loop in the hybrid domain. Using pHluorin as a pH-sensitive ecto-tag provided the first live images of fusion of $\beta 1$ integrin-rich vesicles with the plasma membrane, and suggests preferential vesicular fusion in the vicinity of focal adhesions (FAs). Using HaloTag as an enzymatic ecto-tag that covalently binds synthetic chemical ligands²⁴, we selectively labeled cell-surface and intracellular $\beta 1$ integrins with different fluorophores and dynamically followed them simultaneously to illustrate $\beta 1$ integrin internalization and trafficking in cells. We propose that the ecto-tagged integrins described herein will provide new and powerful tools for live imaging of integrins in cells, and will allow for detailed spatiotemporal dissection of integrin trafficking.

Results

Insertion of a tag in the $\beta 1$ integrin ectodomain. To generate new tools that facilitate imaging of integrins and their trafficking, we set out to introduce tags into the extracellular domains of the widely expressed $\beta 1$ integrins. Integrin β subunits contain 8 extracellular domains and notably the three N-terminal domains are nested within one another (Fig. 1a). Several factors restrict the number of suitable sites for placement of a large tag such as GFP, Halo or SNAP: (i) the large aforementioned nested N-terminal domains, (ii) the presence of an N-terminal signal peptide that gets cleaved off during polypeptide maturation, (iii) the need to retain the ability to pair with integrin α subunits to bind ligand, and (iv) the need to accommodate the large-scale conformational rearrangements thought to occur during integrin activation. Thus, finding a suitable non-perturbing site is far from trivial.

To identify suitable tagging sites we examined published crystal structures of headpiece fragments of $\alpha 5\beta 1$ ²⁵, and both headpiece and full-length ectodomains of $\alpha v\beta 3$ ^{26–29} and $\alpha IIb\beta 3$ ^{6, 30–34} alone or in complex with inhibitors or ligands. We sought a surface loop that was consistently exposed in full-length bent structures as well as active headpiece structures, and which was far enough away from the ligand-binding site that it would be unlikely to clash with bound ligand. We selected a long exposed loop ($\beta 1$ residues 92–114) between β strands X and A (following the nomenclature of Xiong et al.²⁶) in the hybrid domain (Fig. 1b). This loop was exposed in the crystal structures of $\alpha IIb\beta 3$ and $\alpha v\beta 3$ integrins. Furthermore, although this loop is shorter in $\beta 2$ integrins it is located in a similar exposed position in structures of the full-length bent inactive $\alpha x\beta 2$ ³⁵. Notably, the loop lies within the hybrid domain, which undergoes substantial motion during activation and ligand binding, increasing the risk that tags may alter the activation/inactivation equilibrium. Indeed, the allosteric

inhibitory $\beta 1$ antibody SD/19 binds to this loop and a SD/19 Fab was co-crystallized with the $\alpha 5\beta 1$ headpiece²⁵. However, SD/19 also makes contacts with the β subunit A domain and probably inhibits ligand binding by wedging between the β A-domain and the hybrid domain, preventing the swing-out of the hybrid domain required for ligand binding²⁵. We therefore hypothesized that inserting a tag with a flexible linker into this exposed loop (residues 92–114) would be accommodated.

To generate ‘ecto-tagged’ $\beta 1$ integrins, we introduced unique restriction sites into a human $\beta 1$ cDNA between the codons for Gly101 and Tyr102 and inserted PCR-amplified GFP, pHluorin, SNAP, or Halo sequences at these sites, along with 4- or 9-amino acid flexible linkers on both sides (Fig. 1c). As controls we used untagged human $\beta 1$ integrin and a previously described $\beta 1$ integrin containing a GFP fused to the C-terminus of the cytoplasmic tail^{21, 36}. All expression constructs were introduced into pLENTI lentiviral expression vectors for transduction of target cells.

Ecto-tag $\beta 1$ integrins are expressed at the cell surface. To test if ecto-tagged $\beta 1$ integrins are functional, we reconstituted $\beta 1$ integrin knockout (KO) mouse fibroblasts with ectopically expressed ecto-tagged human $\beta 1$ integrins, or for comparison, untagged (no-tag) or cytoplasmically-tagged (cyto-GFP) $\beta 1$ integrins. Flow cytometry confirmed that the clonal line of CRE-infected $\beta 1$ integrin KO cells lacks surface mouse $\beta 1$ integrin, when compared with parental $\beta 1$ integrin floxed fibroblasts (fl/fl) and control unstained KO fibroblasts (Ctrl; Fig. 2a). Following stable lentiviral-mediated transduction of the $\beta 1$ integrin KO fibroblasts with our human $\beta 1$ integrin expression constructs, or with GFP alone, we assessed $\beta 1$ expression by immunoblotting whole-cell lysates using an antibody that detects both mouse and human $\beta 1$ integrin (Fig. 2b). As expected, $\beta 1$ integrin was detected in parental $\beta 1$ integrin fl/fl fibroblasts but not in $\beta 1$ integrin KO cells. Using the same anti- $\beta 1$ integrin antibody we detected all ectopically expressed human $\beta 1$ integrins at their expected molecular weight. Furthermore, immunoblotting with an anti-GFP antibody detected GFP- and pHluorin-tagged integrins. Importantly, in most cases the ectopically expressed integrins appear to be intact with little or no degradation fragments evident. Although the anti- $\beta 1$ integrin antibody bound both mouse and human $\beta 1$ integrins, it may not do so equally, making it impossible to directly compare expression levels of the ectopically expressed human integrins and endogenous mouse integrins.

To test whether tagged integrins were expressed at the cell surface, we assessed human $\beta 1$ integrin levels in reconstituted fibroblasts by flow cytometry with the anti-human $\beta 1$ integrin antibody P5D2. As expected, parental fl/fl and KO cells as well as KO cells expressing GFP alone lacked human $\beta 1$ (Fig. 2c, upper panel). Cell-surface $\beta 1$ integrins were detected in all reconstituted lines. Notably, with the exception of cells expressing ecto-SNAP $\beta 1$ integrin where surface $\beta 1$ integrin expression was low and heterogeneous, all other $\beta 1$ -expressing lines appeared as single populations with relatively homogeneous $\beta 1$ integrin surface levels. Moreover, cells reconstituted with GFP or with $\beta 1$ integrin carrying GFP or pHluorin tags exhibited GFP fluorescence (Fig. 2c, lower panel), indicating that the fluorescent protein was properly folded when inserted into $\beta 1$ integrin ectodomain. We thus conclude that $\beta 1$ integrins with a GFP, pHluorin, or Halo tag inserted into the βX - βA loop of the hybrid domain are expressed and are effectively targeted to the plasma membrane. Notably, the length of the spacer (4 or 9 amino acids) had little impact on expression or targeting. While SNAP-tagged $\beta 1$ integrin is expressed, little reaches the plasma membrane and we suspect that defective folding or aggregation leads to its accumulation in

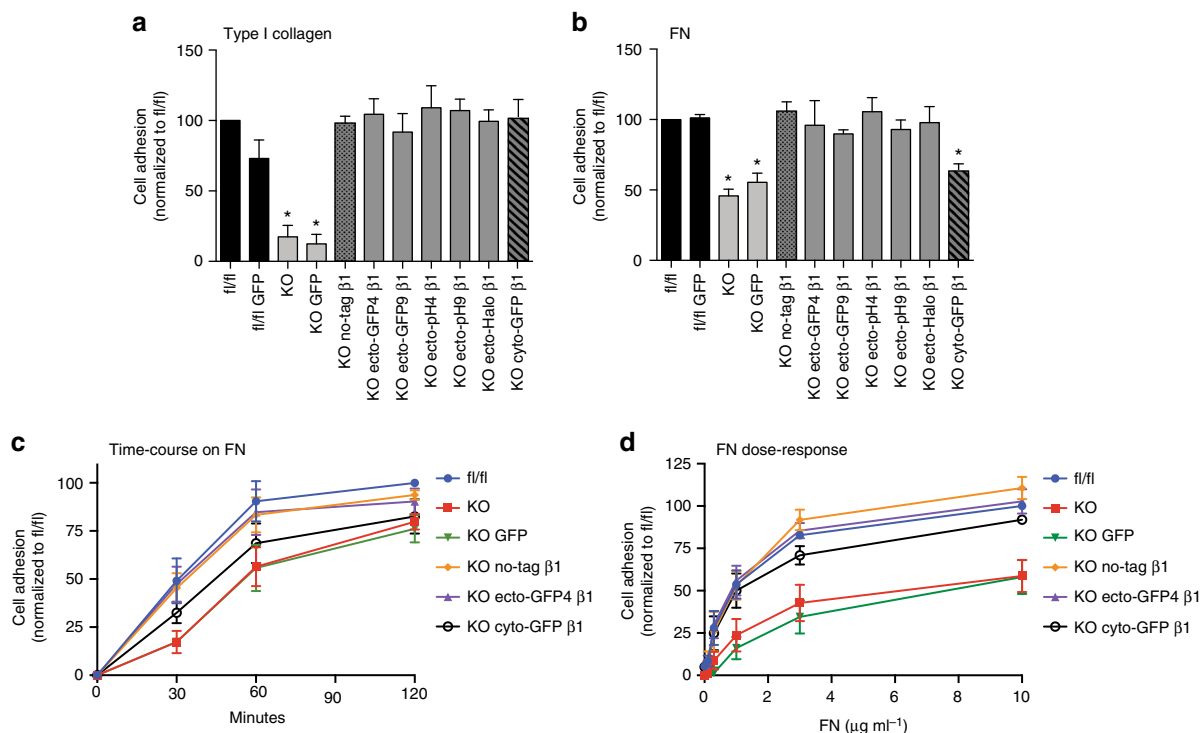


Fig. 3 Ecto-tagged $\beta 1$ integrins rescue the adhesion defect of $\beta 1$ integrin KO fibroblasts. **a** Adhesion of parental and reconstituted $\beta 1$ integrin fl/fl and KO fibroblasts 2 h after plating on wells coated with $3 \mu\text{g ml}^{-1}$ type I collagen. **b** Adhesion of parental and reconstituted $\beta 1$ integrin fl/fl and KO fibroblasts 1 h after plating on wells coated with $3 \mu\text{g ml}^{-1}$ FN. **c** Time course of adhesion of parental and reconstituted $\beta 1$ integrin fl/fl and KO fibroblasts on wells coated with $3 \mu\text{g ml}^{-1}$ FN. **d** Dose-response adhesion assay of parental and reconstituted $\beta 1$ integrin fl/fl and KO fibroblasts for 1 h to wells coated with increasing concentrations of FN. In all experiments, cell adhesion was measured by the absorbance at 570 nm after Crystal Violet staining. Data is shown as mean \pm SEM from three independent experiments. In **a**, **b**, statistical analysis was performed using one-way repeated measures ANOVA with Dunnett post hoc test. Each column was compared to fl/fl and $*p < 0.05$

the endoplasmic reticulum (ER). For this reason the ecto-SNAP $\beta 1$ integrin was not characterized further.

Ecto-tag $\beta 1$ integrins target to focal adhesions. In adherent fibroblasts, integrins cluster at cell-matrix adhesion sites—most notably FAs—where they co-localize with a range of cytoplasmic and cytoskeletal proteins. We therefore investigated whether ecto-tagged $\beta 1$ integrins localized to FAs in reconstituted $\beta 1$ integrin KO fibroblasts plated on fibronectin (FN)-coated coverslips. Immunofluorescence using the conformation-specific antibody 9EG7, which recognizes active $\beta 1$ integrins³⁷, showed that all ectopically expressed human $\beta 1$ integrins (no-tag, ecto-tag, and cyto-GFP) co-localized with the FA marker vinculin, just like endogenous mouse $\beta 1$ integrin in parental fl/fl cells (Fig. 2d). We did not observe any obvious effect of the tags on FA size or number, which were highly variable in our fibroblast population. As expected, no $\beta 1$ integrin signal was detected in parental KO cells or KO cells expressing GFP alone, although these cells still formed vinculin-rich FAs, presumably via endogenous $\alpha\beta 3$ or $\alpha\beta 5$ integrins³⁸. GFP fluorescence could also be detected in FAs in cells expressing human $\beta 1$ integrins carrying a GFP or pHluorin tag, indicating that their fluorescent tag was functional.

The preceding data show that ecto-tagged integrins localize normally to FAs. However, to assess whether they exhibit defective maturation or accumulate in the ER we performed immunofluorescence with the activation-insensitive anti- $\beta 1$ antibody AIIB2³⁹. AIIB2 staining confirmed that ectopically expressed human $\beta 1$ integrins (no-tag, ecto-tag, and cyto-GFP) co-localize with FA markers but also revealed more intracellular staining than seen with the activation-specific anti- $\beta 1$ antibody

9EG7, consistent with some ER accumulation (Supplementary Fig. 1a). This intracellular staining was evident with all exogenously expressed integrins, regardless of whether they contained an ecto-tag, cyto-tag, or no-tag, indicating that the ecto-tag does not cause a maturation defect. To test whether the intracellular staining is related to integrin expression levels we varied the quantity of virus used to drive $\beta 1$ expression. We observed that lowering expression levels reduced the intracellular signal while retaining adhesion targeting for all $\beta 1$ integrins tested, tagged or not (Supplementary Fig. 1b). Consistent with this, flow cytometry showed that diluting the virus reduced cell-surface expression of both no-tag and ecto-GFP4 $\beta 1$ integrins proportionately, and also reduced total GFP signal for ecto-GFP4 $\beta 1$ (Supplementary Fig. 1c). However, the ratio of cell surface ecto-GFP4 $\beta 1$ to total GFP signal increased at lower viral titers indicating that, at lower integrin expression levels, a greater percentage is present on the cell surface (Supplementary Fig. 1d). Together these data show that ecto-tagged integrins traffic efficiently to the cell surface where they form adhesions, and that when expressed at appropriate levels they do not aberrantly accumulate inside the cell.

To examine a larger spectrum of adhesions, we imaged $\beta 1$ KO fibroblasts stably co-expressing the adhesion marker paxillin-mCherry and various ecto-tagged or no-tag $\beta 1$ integrins. Cells were plated on FN-coated glass-bottomed plates and adhesions examined 1 h (Supplementary Fig. 2a) or 24 h (Supplementary Fig. 2b) after plating. In all cases, co-localization of ecto-tagged and untagged integrins with paxillin-mCherry was evident in nascent adhesions (Supplementary Fig. 2a), mature FAs, and fibrillar adhesions (Supplementary Fig. 2b). Ecto-tagged integrins also co-localized with paxillin-mCherry in FAs in cells plated on type I

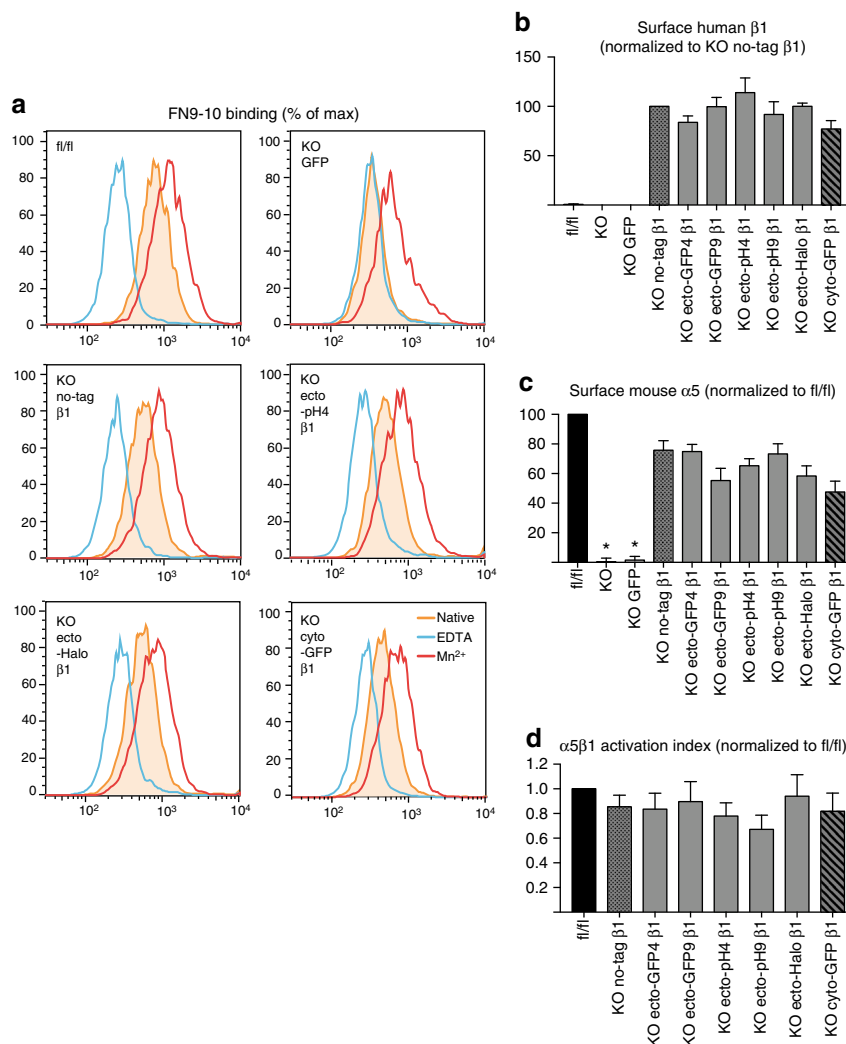


Fig. 4 Ecto-tagged $\beta 1$ integrins bind soluble ligand, restore surface levels of endogenous $\alpha 5$ integrins, and display normal activation indices. **a** Flow cytometry histograms showing binding of soluble FN9-10 to parental and a subset of reconstituted KO fibroblasts, in native conditions (filled orange peak), EDTA-inhibited conditions (blue peak), or Mn^{2+} -treated conditions (red peak). Full data set in Supplementary Fig. 3a. **b**, **c** Quantification of surface levels of human $\beta 1$ (**b**) and mouse $\alpha 5$ integrins (**c**) measured by flow cytometry on parental and reconstituted $\beta 1$ integrin fl/fl and KO fibroblasts. **d** Activation index of surface $\alpha 5\beta 1$ integrins on parental and reconstituted $\beta 1$ integrin fl/fl and KO fibroblasts, calculated as (FN9-10 binding in native conditions—FN9-10 binding in EDTA-inhibited conditions)/surface levels of $\alpha 5$ integrins. All data **b-d** is shown as mean \pm SEM from four independent experiments. Statistical analysis was performed using one-way repeated measures ANOVA with Dunnett post hoc test. Each column was compared to KO no-tag $\beta 1$ and * $p < 0.05$

collagen (Supplementary Fig. 2c) and ecto-Halo $\beta 1$ integrins localized in FA in HeLa cells also expressing endogenous $\beta 1$ integrins (Supplementary Fig. 2d). Thus, inserting an ecto-tag into human $\beta 1$ integrin hybrid domain did not impair targeting to a spectrum of adhesions on a range of integrin substrates.

Ecto-tag $\beta 1$ integrins rescue adhesion in $\beta 1$ -null fibroblasts.

Our results indicate that ecto-tagged integrins are expressed, traffic to the plasma membrane, and localize to FAs, suggesting that these integrins are functional. To test this further we assessed whether they could restore normal adhesion in $\beta 1$ integrin KO cells. $\beta 1$ -containing integrins are major collagen receptors in fibroblasts, and consistent with this, compared to parental $\beta 1$ integrin fl/fl fibroblasts, $\beta 1$ integrin null fibroblasts exhibited severely impaired adhesion to plates coated with $3 \mu g ml^{-1}$ type I collagen (Fig. 3a). When $\beta 1$ integrin KO fibroblasts were reconstituted with untagged, ecto- or cyto-tagged human $\beta 1$, adhesion to collagen was fully restored to levels seen with $\beta 1$ integrin fl/fl fibroblasts, while GFP alone had no effect (Fig. 3a). Similar results

were observed with FN-coated plates; however, in this case KO cells exhibited only $\sim 50\%$ inhibition in adhesion, and the $\beta 1$ cyto-GFP construct was unable to fully rescue adhesion (Fig. 3b). It is likely that, in the absence of $\alpha 5\beta 1$, KO cells adhere via $\alpha v\beta 3$ or $\alpha v\beta 5$ integrins³⁸, explaining the partial adhesion defect. To examine this further, we performed time-course (Fig. 3c) and dose-response (Fig. 3d) adhesion assays on FN comparing the ability of no-tag, ecto-GFP4, and cyto-GFP $\beta 1$ integrins to rescue cell adhesion. Results showed that ecto-GFP4 $\beta 1$ and no-tag $\beta 1$ were practically undistinguishable at all time points and all FN doses tested, while cyto-GFP $\beta 1$ integrin exhibited only a very small temporary lag in adhesion. Thus, insertion of an ecto-tag in $\beta 1$ integrin hybrid domain preserves function.

Ecto-tag $\beta 1$ integrins are active. One concern with inserting tags in the hybrid domain is that it may alter integrin activation, perhaps by stabilizing extended active structures leading to hyper-activation of integrins. The similar adhesion of cells expressing untagged and ecto-tagged integrins (Fig. 3) suggests

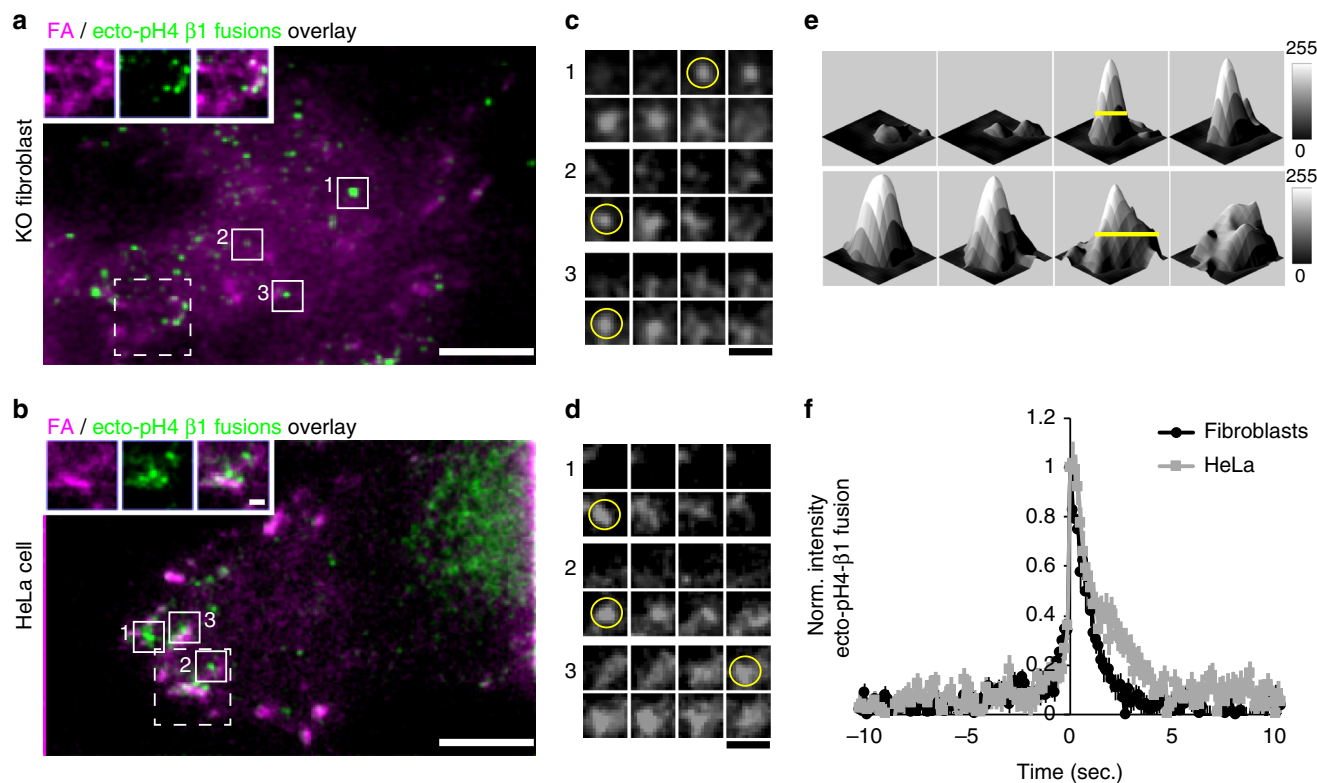


Fig. 5 Visualization of ecto-pHluorin- $\beta 1$ integrin exocytosis in live cells by TIRFM. **a, b** Overlay images of ecto-pH4 $\beta 1$ integrins prior to photobleaching to mark the footprint of FA (magenta) in KO fibroblasts reconstituted with ecto-pH4 $\beta 1$ integrin (**a**) or HeLa cells overexpressing ecto-pH4 $\beta 1$ integrin (**b**), and the maximum projection of ecto-pH4 $\beta 1$ integrin fusion events after photobleaching (fusions, green label; Supplementary Movies 1 and 2). Scale bar, 10 μm . Top left corner insets show fusion events (green) in close proximity to FA (magenta) (**a, b**; dashed line square). Scale bar, 2 μm . **c, d**, Galleries of single ecto-pH4 $\beta 1$ integrin fusion events over time (solid squares on **a, b**; 0.25 s between images). Yellow circle denotes event in which the vesicle signal intensity of the ecto-pH4 $\beta 1$ integrin fluorescence rapidly intensifies, likely due to de-acidification upon opening of the fusion pore. Scale bar, 2.5 μm . **e** Surface plot analysis of a fusion event showing the increase on the full-width half maximum (FWHM) of the signal peak over time, consistent with bona fide full vesicle fusion (yellow lines; 0.25 s between plots). **f** Temporal alignment of fusion events detected on reconstituted KO fibroblasts (black line) or HeLa cells (gray line) cells showed the expected changes in ecto-pH4 $\beta 1$ integrin during fusion. Data are shown as mean \pm SEM for 67 and 44 events, respectively (2 cells for each)

that this is not the case, but to directly test this question we assessed binding of a soluble FN fragment containing FN type III repeats 9 and 10 (FN9-10) in a well-established flow cytometric assay⁴⁰. Fl/fl fibroblasts displayed clear binding of FN9-10 (Fig. 4a, orange shaded peak) that was both inhibited by ethylenediaminetetraacetic acid (EDTA; blue peak) and stimulated by Manganese (Mn^{2+} , red peak). Specific binding of FN9-10 (native binding—binding in EDTA) was greatly reduced in GFP-expressing $\beta 1$ KO cells, as binding in native condition was very similar to binding in EDTA-treated condition (Fig. 4a). Notably, while expression of GFP alone had no effect, specific binding of soluble FN9-10 was restored when $\beta 1$ integrin KO cells were reconstituted with any of the human $\beta 1$ integrins (no-tag, cyto-GFP, and ecto-tags) as evidenced by the higher FN9-10 binding in native vs. EDTA-treated conditions (Fig. 4a and Supplementary Fig. 3a). Moreover, FN9-10 binding in reconstituted cells was enhanced by manganese.

Hence our data indicate that introducing a GFP, pHluorin, or Halo tag in $\beta 1$ integrin hybrid domain is compatible with ligand binding and does not interfere with its regulation by EDTA or manganese. To quantify integrin activation we measured specific binding and normalized it to integrin expression levels. Although all the reconstituted cells exhibited comparable levels of human $\beta 1$ integrin (Fig. 4b), due to antibody specificity, we were unable to directly compare levels of human $\beta 1$ integrins in reconstituted cells with levels of endogenous mouse $\beta 1$ integrin in fl/fl cells. To circumvent this problem, we measured surface levels of

endogenous mouse $\alpha 5$ integrin as a means to assess surface $\alpha 5\beta 1$ levels. Mouse $\alpha 5$ integrin, an obligate $\beta 1$ integrin partner, was present at the surface of $\beta 1$ integrin fl/fl cells but not at the surface of $\beta 1$ integrin KO cells (Fig. 4c), in agreement with previous data showing that α and β integrin subunits have to heterodimerize in order to be transported to the cell surface. Importantly, in $\beta 1$ integrin KO cells, $\alpha 5$ surface levels were rescued by ectopic expression of any of the human $\beta 1$ integrins (Fig. 4c). Notably, $\alpha 5$ surface levels did not quite reach the levels observed in $\beta 1$ integrin fl/fl cells, and we speculate that this could be either due to a suboptimal pairing of mouse $\alpha 5$ with human $\beta 1$ integrin subunits or due to differences in $\alpha 5$ levels between the clonal $\beta 1$ integrin KO line and the parental polyclonal $\beta 1$ integrin fl/fl cell population. Nonetheless, when surface levels of $\alpha 5$ were used to calculate the activation index of $\alpha 5\beta 1$ (specific binding normalized by integrin expression), we found that cells reconstituted with no-tag $\beta 1$, cyto-GFP $\beta 1$, or ecto-tag $\beta 1$ all had similar activation indices, only slightly below that of parental fl/fl cells (Fig. 4d). In addition, the activation-specific hybrid domain-binding antibody HUTS-4⁴¹ bound equivalently to both untagged and ecto-tagged integrins (Supplementary Fig. 3b). Therefore we conclude that $\alpha 5\beta 1$ integrin dimers containing ecto-tag $\beta 1$ integrins are not hyperactivated when compared with either $\alpha 5\beta 1$ integrins containing untagged human $\beta 1$ or with endogenous mouse $\alpha 5\beta 1$ integrins, suggesting that the insertion of the tag into the hybrid domain does not substantially interfere with the processes of activation and inactivation.

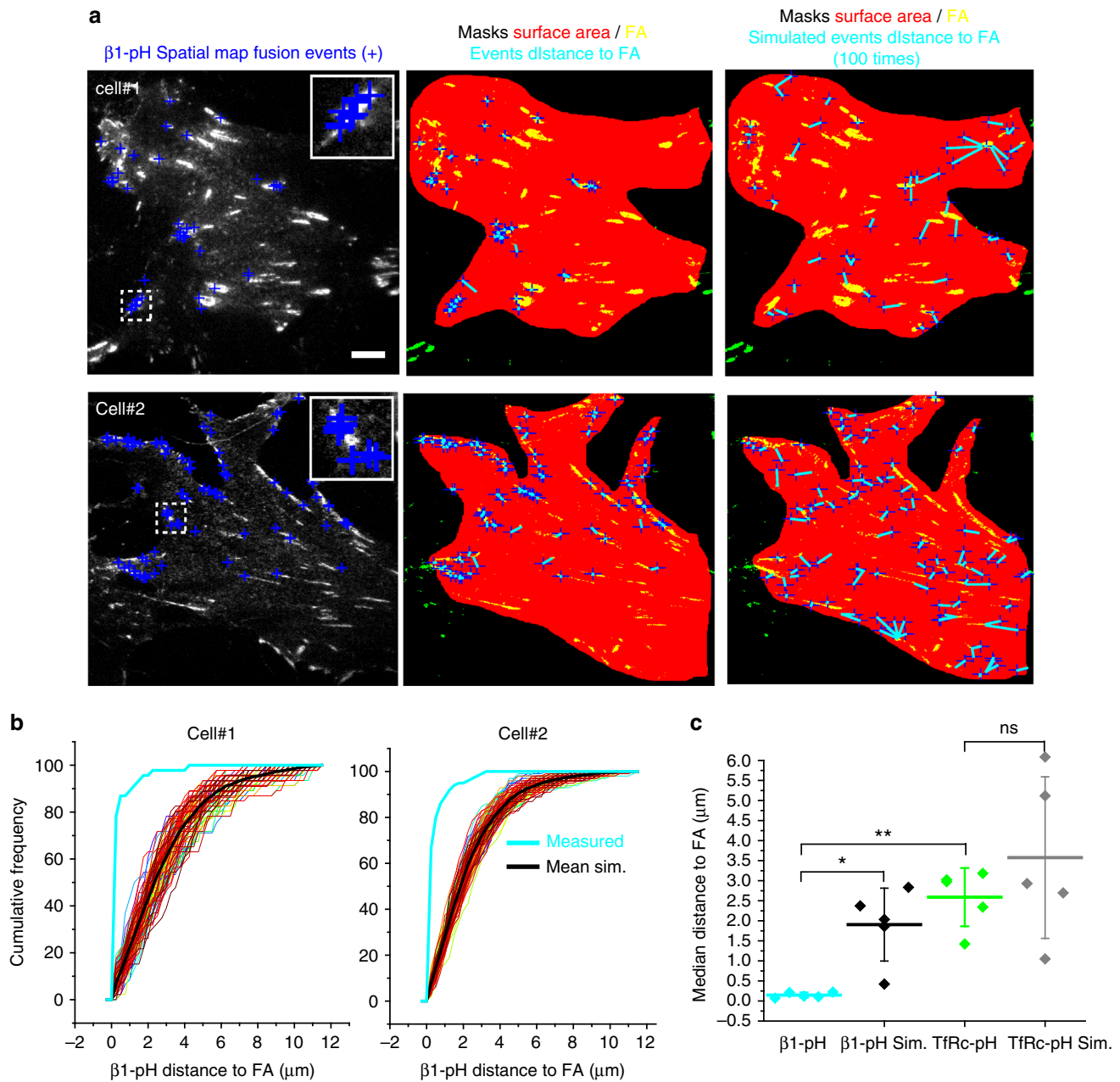


Fig. 6 Spatial distribution analysis of ecto-pH4 $\beta 1$ integrin fusion events supports direct integrin delivery to FAs. **a** *Left panel*, Distribution of fusion events (blue crosses) and FAs (white) detected by TIRFM in two KO fibroblasts reconstituted with ecto-pH4 $\beta 1$ integrins ($\beta 1$ -pH). *Center panel*, the distance of fusion events to the nearest FA (yellow mask) was measured (cyan lines). *Right panel*, the distance of randomly simulated events around the cell surface (red mask) to the nearest FA were measured (cyan lines). Scale bar, 10 μm . **b** Cumulative frequency charts for the two cells demonstrating the difference in distance to FA between the measured data (cyan line) and 100 simulations (individual simulation, color lines; mean, black line). **c** Quantification of the median distance to FAs for $\beta 1$ -pH or TfRc-pH fusion events, and the simulations ($\beta 1$ -pH Sim and TfRc-pH Sim) performed in the same cells. The scatter-box graph shows the mean \pm SD for 5 cells and the respective simulation data. Statistical analysis was performed using a two samples Student's *t*-test. * $p < 0.05$, ** $p < 0.01$

Live imaging of pHluorin- $\beta 1$ integrin exocytosis. Having established the functionality of ecto-tagged $\beta 1$ integrins, we sought to take advantage of the pH sensitivity of pHluorin fluorescence to visualize integrin exocytosis in live cells. Based on our experience with previously generated ecto-pHluorin-tagged membrane proteins^{42–44}, we predicted that (1) ecto-pHluorin $\beta 1$ integrins would emit little fluorescence in secretory vesicles due to the quenching of ecliptic pHluorin at acidic pH, and that (2) during exocytosis, ecto-pHluorin $\beta 1$ integrin-loaded secretory vesicles fusing with the plasma membrane would expose their cargo to the neutral extracellular environment (pH~7.4) resulting

in a burst of green fluorescence. This burst of fluorescence is expected to be transient due to the rapid diffusion of the pHluorin cargo in the plasma membrane.

Live $\beta 1$ integrin KO fibroblasts re-expressing ecto-pHluorin $\beta 1$ integrin were imaged by TIRFM to visualize pHluorin- $\beta 1$ integrin exocytosis at the plasma membrane-matrix interface (Fig. 5a)^{43, 44}. Live-cell TIRFM imaging confirmed our observation in fixed cells that pHluorin- $\beta 1$ integrin localized to FAs (Fig. 5a, magenta label). Similar results were obtained in HeLa cells stably expressing pHluorin- $\beta 1$ integrin on a wild-type $\beta 1$ integrin background (Fig. 5b), supporting that our constructs

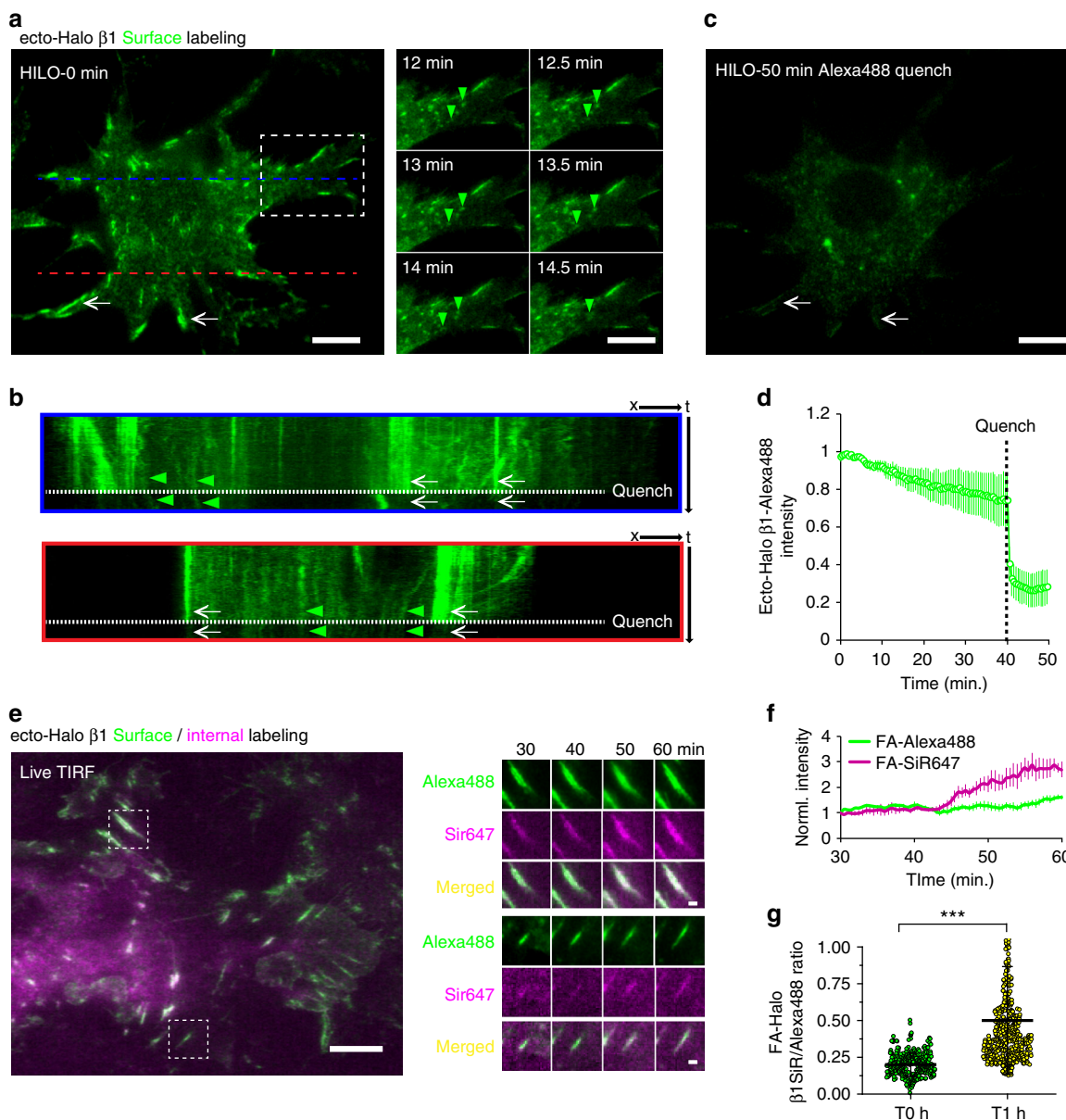


Fig. 7 Selective surface and internal labeling of ecto-Halo $\beta 1$ integrins demonstrates integrin endocytosis in live cells. **a** Labeling of surface ecto-Halo $\beta 1$ integrins in reconstituted KO fibroblasts with Alexa488 Halo ligand and imaging by HILO TIRFM immediately after labeling (0 min). Scale bar, 15 μm . Right panel, movement of Alexa488-positive vesicle-like structures (dashed line rectangle, green arrowheads). Scale bar, 10 μm . **b** Kymograph of two regions of the cell (blue and red lines) illustrating the dynamics of Alexa488-positive structures before (green arrowheads) and after the addition of Alexa488 quencher antibody (white arrows). **c** Residual Alexa488 signal after quenching, imaged by HILO TIRFM 50 min post labeling (white arrows). Scale bar, 15 μm . **d** quantification of normalized ecto-Halo $\beta 1$ Alexa488 intensity before and after quenching. The line graph shows the mean \pm SD of the normalized intensity for 5 cells. **e** Overlay image of KO fibroblasts reconstituted with ecto-Halo $\beta 1$ integrins, after sequential labeling with Alexa488 and SiR647 Halo ligands and imaged by TIRFM. Scale bar, 15 μm . Images on the right show the time series of two FAs (dashed line square). Scale bar, 2.5 μm . **f** Line graph showing the temporal changes in SiR647 and Alexa488 Halo signals in FAs measured by TIRFM during a 30 min period (mean \pm SD for 4 FAs). **g** Scatter-box graph showing the mean \pm SD for the ratio of SiR647/Alexa488 Halo signals of 388 and 523 FAs imaged by TIRFM 0 h or 1 h after incubation at 37 $^{\circ}\text{C}$ on fixed samples (6 cells per conditions). Statistical analysis was performed using a two samples Student's *t*-test and ****p* < 0.001

are effective in different cell types and can be applied even in the presence of endogenous $\beta 1$ integrin. Photobleaching of the background surface signal (Supplementary Fig. 4) allowed us to visualize for the first time pHluorin- $\beta 1$ integrin exocytosis events (Fig. 5a, b, green label; Supplementary Movies 1–2). Critically, pHluorin- $\beta 1$ integrin cargo incorporated and dispersed into the plasma membrane in a manner that shows a clear signature of exocytic fusion⁴³: (1) a rapid increase in signal when a pHluorin cargo-loaded vesicle de-acidified (Fig. 5c, d; yellow circles), (2) the full-width half maximum (FWHM) of the signal peak increased

over time (Fig. 5e, yellow lines), and (3) the average vesicular profile of multiple fusion events ($n = 44$ –67), which were time-aligned to fusion, showed the expected intensity spread during exocytosis⁴³ (Fig. 5f). Notably, this approach allowed us to visualize pHluorin- $\beta 1$ integrin exocytosis events, which appeared to occur preferentially near FAs (Fig. 5a, b, dashed line square; inset).

Integrin association with specific vesicular adapters of the trafficking machinery suggests that their delivery to particular areas on the cell is spatially regulated, and we therefore sought to

rigorously test the hypothesis that integrin exocytosis might preferentially occur in close proximity to existing FAs. To test this hypothesis, we generated spatial maps of integrin fusion events from 5 cells (Supplementary Fig. 5a) and overlaid them relative to a FA map (Fig. 6a, *yellow mask*). Here too, fusion events appeared to cluster in close proximity to FAs (Fig. 6a, *inset blue crosses*). To statistically test this concept, Monte Carlo simulations were used to randomly assign the same number of events throughout the cell surface area imaged by TIRFM (Fig. 6a, *red mask*)^{45,46}. Using a custom algorithm we computed the distance of each event to the closest FA in both the real data and after 100 Monte Carlo simulations (Fig. 6b), which showed that pHluorin- $\beta 1$ integrin ($\beta 1$ -pH) fusion events were highly clustered near FAs (Fig. 6b, *cyan line*) while simulated events were more randomly scattered on the cell surface (Fig. 6b, *black line*). Interestingly, only a subset of the FAs appeared to be targeted by fusion events, even in these non-polarized cells. When combined from 5 different cells, measurements of the median distance to FAs was strikingly different between $\beta 1$ -pH fusion events and simulated events (Fig. 6c), with $\beta 1$ -pH showing an average distance of $<0.25 \mu\text{m}$ compared to $\sim 2 \mu\text{m}$ in the simulations—strongly supporting a model of preferential delivery of integrins to FAs.

For comparison and to test the possibility that the clustering of integrin fusion events at FAs could be due to a distance artifact (the cell membrane is closer to glass at FAs than in the rest of the cell^{47, 48}), we analyzed the spatial distribution of transferrin receptor-pHluorin (TfRc-pH) fusion events from 5 cells expressing the FA maker Paxillin-mCherry. Fusion events exhibited the expected signature of pHluorin-tagged cargo delivered to the cell surface and were distributed along the ventral cell surface (Supplementary Fig. 5b). Mapping analysis of the distance of TfRc-pH fusion events to FAs showed that these events occur over 10-fold further away from FAs than the $\beta 1$ -pH events (Fig. 6c; Supplementary Fig. 6; *cyan vs. green line*). In fact, the distance to FAs measured for TfRc-pH fusion events was not significantly different from that of randomly occurring simulated events in the same cells (Fig. 6c; Supplementary Fig. 6; *green vs. gray line*). Together, these findings support that exocytosis of $\beta 1$ -integrin, but not a general recycling cargo, shows a high spatial selectivity for fusion at FAs.

Our analysis of pHluorin-tagged $\beta 1$ integrin exocytosis provides the first direct, quantitative evidence for targeted delivery of integrin-rich vesicles to FAs. The mechanism by which this spatial targeting is achieved is unknown, but prior reports have shown accumulation of integrins in FAs at the leading edge of migrating cells in a phosphoinositide-regulated exocyst-complex-dependent manner⁴⁹, and our ecto-tagged integrins provide a powerful tool for future investigation of this process.

Dynamic live imaging of Halo- $\beta 1$ integrin endocytosis. Integrin endocytosis and recycling is another important aspect of integrin traffic. When assessed biochemically using reversible cell-surface biotinylation, Ecto-GFP4 $\beta 1$ (Supplementary Fig. 7a, b) and ecto-Halo $\beta 1$ (Supplementary Fig. 7c, d) internalized at rates comparable to untagged $\beta 1$ integrins. To assess ecto-Halo $\beta 1$ endocytosis by live cell imaging we took advantage of the interchangeable chemical-genetic labeling technology of HaloTag, a modified haloalkane dehalogenase that covalently binds synthetic small-molecule ligands which can be coupled to fluorophores or other affinity tags^{24, 50, 51}. Importantly, both membrane-permeant and -impermeant fluorescent Halo substrates are commercially available (e.g., Promega). First, we specifically and selectively labeled surface ecto-Halo $\beta 1$ integrins in live $\beta 1$ integrin KO fibroblasts with the cell-impermeant HaloTag Alexa Fluor 488 Ligand (Fig. 7a; Supplementary Fig. 8a). Determining

the levels of labeled ecto-Halo $\beta 1$ integrins endocytosis in live cells by TIRFM imaging can be a challenge since: (1) TIRFM illumination only excites the labeled integrins close to the glass surface, and (2) the high levels of labeled integrins at the surface can mask the detection of dimmer internal structures. To overcome these challenges (1) we used highly inclined and laminated optical sheet (HILO) illumination⁵² to obtain deeper images of labeled ecto-Halo $\beta 1$ integrins in cells and with a better signal/noise ratio than spinning disk confocal and (2) we quenched surface fluorescence by treating cells with an antibody against Alexa488 to unmask internalized labeled integrins⁵³ (Fig. 7a, c; Supplementary Movie 3). The HILO illumination approach allowed us to visualize the appearance of Alexa488-positive vesicle-like structures inside the cells (Fig. 7a; *right panel, green arrow heads*), which displayed curvilinear tracks and ‘squiggles’ as seen by kymographs (Fig. 7b, *green arrowheads*; focal adhesions (white arrows) hardly moved). After imaging for 40 min, the surface fluorescence was quenched in living cells with the anti-Alexa488 antibody, as evidenced by the strong decrease in signal at the cell surface and at FAs (Fig. 7b, c; *white arrows*). Residual Alexa488 signal remaining after quenching was in small vesicle-like structures inside the cell, which continued to move (Fig. 7b, c). Quantification of the normalized integrin labeling intensity of 5 cells before vs. after quenching (Fig. 7d) supports that 20–25% of the surface ecto-Halo $\beta 1$ integrin signal had endocytosed in 40 min, a value that agrees with the internalization rate of Halo-tagged $\beta 1$ integrins measured biochemically (Supplementary Fig. 7c, d). Further supporting that a portion of ecto-Halo $\beta 1$ was endocytosed, we observed partial co-localization with pulse-labeled (30 min) transferrin-Alexa568 (Tf568; Supplementary Fig. 9a, b).

We then explored the potential of using HaloTag ligands with distinct properties to label various pools of $\beta 1$ integrins in cells. We used a sequential labeling strategy to separately label surface and internal pools of ecto-Halo $\beta 1$ integrins in live cells. We first incubated ecto-Halo $\beta 1$ integrin-reconstituted KO fibroblasts with the cell-impermeant Alexa488 Halo Ligand and then with the cell-permeant SiR647 Halo ligand, with the expectation that prior incubation with Alexa488 Halo ligand would saturate surface Halo sites, resulting in intracellular-only labeling with SiR647 Halo ligand. Indeed, the Alexa488 Halo ligand labeled surface ecto-Halo $\beta 1$ integrins present in FAs (Supplementary Fig. 9c, *green label, green arrowheads*) and stained the ventral and dorsal surface of the cell (Supplementary Fig. 9e). In contrast, the SiR647 Halo ligand did not label FAs (Supplementary Fig. 9c T0h, *magenta label*), rather it stained an internal pool of $\beta 1$ integrins (Supplementary Fig. 9e), mainly in the ER, the Golgi, and endosomes (Supplementary Fig. 8b). We then examined the long-term changes in subcellular localization of these two pools of $\beta 1$ integrins. 16 h after sequential Halo labeling, Alexa488-positive intracellular vesicular structures were visible by confocal microscopy (Supplementary Fig. 9d, *green label, right bottom panel*), indicating that some surface $\beta 1$ integrins had been internalized. After 16 h, SiR647-labeled integrins co-localized with Alexa488-labeled integrins in FAs as well as in intracellular structures (Supplementary Fig. 9d, *yellow arrowheads*), indicating that some $\beta 1$ integrins from the intracellular pool at T_0 trafficked to the cell surface and incorporated into FAs. Line scans and Pearson’s correlation analysis confirmed an increase in surface SiR647 staining and co-localization of Alexa488 and SiR647 after 16 h (Supplementary Fig. 9e, f). Interestingly, FAs were still labeled with Alexa488 16 h after labeling (Supplementary Fig. 9d), indicating either a very low internalization rate for surface $\beta 1$ integrins or alternatively a high recycling rate and recruitment into de novo assembled FAs.

To test whether rapid $\beta 1$ integrin recycling takes place, we undertook dual-color labeling, with a sequential 15 min

pre-labeling and live-cell imaging by TIRFM (Fig. 7e–g; Supplementary Movie 4). As expected, at early time points, FAs were mainly labeled by ecto-Halo $\beta 1$ Alexa488, but over a time period of ~30 min FAs were additionally labeled with an intracellular pool of ecto-Halo $\beta 1$ SiR647 (Fig. 7e, f). Quantification of several hundred FAs showed that the labeling with SiR647 increased ~2.5-fold over 1 h, supporting rapid delivery of an internal integrin pool (Fig. 7g). Together, these results demonstrate the feasibility of using ecto-Halo $\beta 1$ integrins in combination with various Halo ligands to selectively label surface and internal pools of integrins, and image and quantify their endocytosis and trafficking in live cells.

Discussion

Endocytosis and exocytosis regulate integrin-mediated adhesion and signaling^{4, 10}. Consequently there is considerable interest in understanding integrin trafficking, with development of innovative tools to follow integrin endocytosis^{11, 15–18}. However, current tools have not allowed direct visualization of exocytosis. Here we describe the design, validation, and application of novel recombinant ecto-tagged $\beta 1$ integrins with tags in an exposed extracellular loop of the $\beta 1$ integrin hybrid domain. We establish that the insertion of GFP, the pH-sensitive GFP variant pHluorin, or the enzymatic tag Halo at this site does not disrupt $\beta 1$ integrin function. Using ecto-pHluorin $\beta 1$ integrin to visualize integrin exocytosis in live cells we reveal preferential delivery of $\beta 1$ integrins to FAs. Furthermore, we show that ecto-Halo $\beta 1$ integrins permit visualization of integrin endocytosis in live cells. We anticipate that future development of cleavable membrane-impermeant Halo ligands should allow discrimination between biosynthetic and recycling pools of integrins and detailed analysis of internalization or recycling kinetics. We initially focused on the $\beta 1$ subunit because it is widely expressed and can pair with a large number of different α subunits, potentially allowing us to investigate a range of integrin heterodimers. However, we note that, as different heterodimers use distinct trafficking pathways¹⁵, the promiscuity of the $\beta 1$ subunit makes discrimination of the routes and kinetics of specific heterodimers difficult to isolate, and in the future specific ecto-tagged α subunits may complement the use of ecto-tagged β subunits. Nonetheless, we anticipate that ecto-tagged $\beta 1$ integrins will provide an important toolkit for integrin research and will greatly facilitate detailed investigation of the integrin trafficking in live cells and potentially in vivo.

Methods

Constructs. Plasmid DNA encoding human $\beta 1$ integrin C-terminally fused to GFP (pcDNA3- $\beta 1$ cyto-GFP)²¹ was provided by Dr. Anthony Koleske (Yale University). An untagged human $\beta 1$ expression construct (pcDNA3 no-tag- $\beta 1$) was generated by subcloning from pcDNA3- $\beta 1$ cyto-GFP. To generate ecto-tagged $\beta 1$ integrin pcDNA3 expression constructs, we used QuikChange Mutagenesis to insert a GAATTCCTCGAG sequence introducing unique EcoRI and XhoI sites into the ecto-domain coding region of pcDNA3 no-tag- $\beta 1$ integrin between codons encoding Gly101 and Tyr102 (Supplementary Table 1). We PCR-amplified eGFP from the pEGFP-C2 vector (Clontech), eGFP-pHluorin from the sspH-mSmo vector⁵⁴, HaloTag from C-Halo vector (Promega) and SNAP from pSNAP β Adrenergic Rc vector (New England BioLabs), using primers that added a 5' linker containing an EcoRI site and a 3' linker containing a XhoI site along with a spacer sequence (Supplementary Table 1). Each ecto-tag was then inserted into the $\beta 1$ integrin ectodomain using the ectopic XhoI-EcoRI sites. We generated ecto-GFP and ecto-pHluorin $\beta 1$ integrin constructs containing either 4 amino acid flanking linkers (ecto-GFP4 and ecto-pH4) or 9 amino acid flanking linkers (ecto-GFP9, ecto-pH9), while ecto-Halo and ecto-SNAP constructs were generated only with 9 amino acid flanking linkers (see Fig. 1 for exact sequence information). A Paxillin-mCherry expression vector was built by PCR and cloning using a *Gallus Gallus* Paxillin-DsRed vector (a gift from Christopher Turner, Upstate Medical University) and pmCherry-N1 (Clontech) as a template for mCherry (Supplementary Table 1).

To generate lentiviral expression vectors, the coding sequence of tagged or untagged $\beta 1$ integrin, GFP or Paxillin-mCherry was PCR amplified with primers designed according to the Gateway Cloning manufacturer's instructions

(ThermoFisher Scientific) to introduce flanking attB1 and attB2 recombination sites (Supplementary Table 1). pENTRY vectors were generated by Gateway BP recombination with pDONR221 and final lentivirus expression vectors were generated by Gateway LR recombination with pLENTI CMV Puro DEST (AddGene plasmid #17452, gift from Eric Campeau). All constructs were verified by DNA sequencing.

Cell culture and transfection. Immortalized $\beta 1$ integrin floxed ($\beta 1$ integrin fl/fl) and Cre-induced $\beta 1$ integrin null ($\beta 1$ integrin KO) fibroblasts³⁶ were provided by Antony Koleske (Yale University) and shown to be mycoplasma free using MycoAlert (Lonza). $\beta 1$ integrin KO cells were cloned by limited dilution and the absence of surface $\beta 1$ integrin in the resulting clonal lines was verified by flow cytometry using a biotinylated anti-CD29 antibody (clone HM $\beta 1$ -1 from Biolegend 112203). Fibroblasts, HEK 293T (a gift from Peter Tattersall, Yale University) and HeLa cells (a gift from Anton Bennett, Yale University) were cultured in Dulbecco modified Eagle medium (DMEM) high glucose containing glutamine supplemented with 9% bovine serum or fetal calf serum, non-essential amino acids and sodium pyruvate. Transfections were performed using PEI (Linear Poly-ethyleneimine MW 25,000, Polysciences, Inc.).

Lentivirus production and infection. Lentiviruses were produced by co-transfecting HEK293T cells with packaging vectors psPAX2 (viral proteins Gag and Rev under the SV40 promoter; Addgene plasmid #12260, a gift from D. Trono, École Polytechnique Fédérale de Lausanne, Lausanne, Switzerland) and pMD2.G (viral protein VSV-G expressed under the CMV promoter; Addgene plasmid #12259, a gift from D. Trono) together with the pLENTI CMV constructs. Viral supernatant was collected 48 and 72 h after transfection and filtered with a 0.45- μ m filter. Cell lines were transduced by incubating with viral supernatant (diluted 1:2 to 1:16) and 8 μ g ml⁻¹ polybrene (Sigma) for 18 h, and selected with puromycin when necessary.

Flow cytometry and analysis of integrin activation. Cell surface levels of human $\beta 1$, mouse $\beta 1$, and mouse $\alpha 5$ integrin were measured by flow cytometry on an LSRII instrument (BD Biosciences) using primary antibodies specific for human $\beta 1$ integrin (P5D2 from Developmental Studies Hybridoma Bank, dilution 1:17; HUTS-4 from EMD Millipore MAB2079Z, dilution 1:1500), mouse $\beta 1$ integrins (biotinylated anti-CD29 clone HM $\beta 1$ -1 from Biolegend 112203, dilution 1:50), and mouse $\alpha 5$ integrin (clone MFR5 from EMD Millipore MABT18, dilution 1:100) followed by either APC-Steptavidin (ThermoFisher Scientific) or Alexa Fluor 647-conjugated anti-mouse or anti-rat secondary antibodies (Invitrogen, dilution 1:500). For control unstained cells, the incubation with primary antibody was omitted.

The activation state of endogenous $\alpha 5\beta 1$ integrins was assessed using a modified version of a previously described flow cytometric assay⁴⁰. Briefly, human FN repeats 9–10 fused to an N-terminal His-tagged Maltose-Binding Protein affinity tag, was purified from *E. Coli* and biotinylated with *N*-hydroxysuccinimidobiotin (ThermoFisher Scientific; FN9–10; manuscript in preparation). Mammalian cells were suspended with trypsin/EDTA, incubated with FN9–10 in the presence or absence of 10 mM EDTA or 0.5 mM MnCl₂, fixed with 4% paraformaldehyde, incubated with APC-Streptavidin and analyzed by flow cytometry on an LSRII instrument (BD Biosciences). The activation index of cells was calculated as $AI = (F - F_0)/F_{\text{integrin}}$, where F is the geometric mean fluorescence intensity (MFI) of FN9–10 binding, F_0 is the MFI of FN9–10 binding in presence of inhibitor, and F_{integrin} is the normalized MFI of anti- $\beta 1$ or anti- $\alpha 5$ integrin antibody binding to cells. Flow cytometry data were analyzed using FlowJo software. Data analysis and statistics were performed using GraphPad Prism.

Adhesion assay. Cell adhesion assays in matrix-coated 96-well plates were based on published protocols⁵⁵. Briefly, Costar flat bottom 96-well plates were coated with FN (0.1–10 μ g ml⁻¹, bovine plasma FN from Sigma) or type I collagen (1–10 μ g ml⁻¹, rat tail collagen from Gibco) and blocked with 10 mg ml⁻¹ heat-denatured BSA (bovine serum albumin fraction V, American Bioanalytical). Cells were plated in replicate wells in serum-free DMEM and returned to 37 °C incubator for 30 min to 3 h. In these conditions, cell adhesion to control uncoated BSA-blocked wells was negligible. At the end of the assay, the wells were carefully washed with PBS, cells were fixed with 5% glutaraldehyde, stained with Crystal Violet, washed, and bound dye was resuspended in 10% acetic acid, as previously described⁵⁵. Absorbance at 570 nm (A) was measured on a Tecan Infinite M200 microplate reader. Background signal (B) corresponded to absorbance in wells stained without cells. In a separate duplicate plate, cells were not washed prior to fixation/staining, and absorbance was used to determine “100% adhesion” (total A). Cell adhesion was calculated as (A–B)/(total A–B). Data analysis and statistics were performed using GraphPad Prism.

Internalization assay. Assessment of integrin internalization was performed as previously described^{56, 57}. Briefly, cell surface proteins were biotinylated on ice with 0.2 mg ml⁻¹ NHS-SS-biotin (Pierce) on ice. After 5–30 min internalization at 37 °C, remaining surface biotin was removed with 50 mM Tris(2-Carboxyethyl) phosphine Hydrochloride (TCEP) and cells were lysed in PBS 0.5% Triton X-100.

Lysates were clarified at $10,000 \times g$ for 10 min and biotinylated proteins were pulled down with Streptavidin agarose beads (Sigma). Pulled-down $\beta 1$ integrins were detected by immunoblotting with anti-CD29 antibody (clone 18 from BD Biosciences 610468, dilution 1:1000). A fraction of each bead supernatant was immunoblotted for β tubulin (clone E7 from Developmental Studies Hybridoma Bank, dilution 1:1000) as a loading control. The amount of $\beta 1$ integrins internalized was calculated as a percentage of total surface signal.

Immunoblotting. Pellets of fibroblasts were resuspended in Laemli Loading Buffer in reducing conditions, passed through a 23G needle 3 times and boiled for 5 min, fractionated by sodium dodecyl sulfate polyacrylamide gel electrophoresis and immunoblotted anti- $\beta 1$ integrin (anti-CD29 clone 18 from BD Biosciences, dilution 1:1000), anti-GFP (Rockland 600-101-215, dilution 1:1000), or anti- β -tubulin (clone E7 from Developmental Studies Hybridoma Bank, dilution 1:1000) antibodies. After incubation with IRDye680 or IRDye800-conjugated secondary antibodies, the signal was scanned on an Odyssey CLx Imaging system, quantified and processed using Image Studio Lite (LI-COR Biosciences). Uncropped images are shown in Supplementary Figs. 10 and 11.

Fluorescence imaging and immunofluorescence. Cells were plated on glass coverslips or glass-bottomed dishes (MatTek) coated with $10 \mu\text{g ml}^{-1}$ FN or $10 \mu\text{g ml}^{-1}$ type I collagen in phenol red-free DMEM culture medium. When specified, live cells were incubated with 250 nM HaloTag Alexa Fluor 488 (Promega) for 30 min at 37 °C. For live imaging, cells were incubated with Prolong Live anti-fade reagent (Invitrogen). Otherwise, for $\beta 1$ integrin and vinculin immunofluorescence, cells were fixed for 30 min with 4% Paraformaldehyde in PBS 0.1% Triton X-100 or in cytoskeletal buffer (10 mM Mes, 150 mM NaCl, 5 mM EGTA, 5 mM glucose, 5 mM MgCl_2 , and pH 6.1) and quenched/blocked with 50 mM NH_4Cl , 0.2% BSA and 0.1% Triton X-100 in PBS. Cells were incubated with anti- $\beta 1$ integrin antibodies (9EG7 from BD Biosciences 553715, dilution 1:300 or AIIB2 from Developmental Studies Hybridoma Bank, dilution 1:200) and an anti-vinculin antibody (hVin1 from Sigma V-9131, dilution 1:10,000), subsequently with Alexa Fluor 488, 568, or 647 secondary antibodies (Invitrogen, dilution 1:500). All fixed cells were mounted in ProLong Diamond anti-fade reagent (Invitrogen) visualized using a Nikon TI microscope under a $\times 100$ immersion oil objective. For ER, endosome, or Golgi immunofluorescence, ecto-Halo $\beta 1$ cells sequentially labeled with Alexa488 and SiR647 Halo ligands were incubated for 1 h at 37 °C after labeling, then washed with PBS, fixed for 20 s in 4% PFA, 0.2% Glutaraldehyde, and 0.1% Triton X-100 and for another 10 min in just 4% PFA and 0.1% Triton X-100. After blocking with 5% BSA PBS, 0.05% Tween 20, the cells were incubated with mouse monoclonal against SERCA2 (ER; Fisher Scientific MA3-919, dilution 1:300), GM130 (cis-Golgi; BD transduction 610823, dilution 1:300), or TfRc (endosomes; Life technologies 136800, dilution 1:300). The cells were then incubated with goat-anti mouse secondary antibody labeled with Alexa568 (dilution 1:1000). The samples were mounted as above and imaged on a Yokogawa-type spinning-disk confocal microscope (SDCM) as described below.

Live-cell imaging. For total internal reflection fluorescence microscopy (TIRFM), ecto-pHluorin $\beta 1$ integrin expressing cells were plated on glass-bottomed dishes (MatTek) coated with $10 \mu\text{g ml}^{-1}$ FN in phenol red-free DMEM supplemented with 9% bovine serum and 25 mM Hepes (imaging medium). Images were acquired on a microscope (IX-70; Olympus) equipped with 488 nm (150 mW) and 568 nm (100 mW) laser lines, temperature-controlled stage set (custom built), a TIRFM condenser (custom condenser), a 60×1.49 NA TIRF objective (Olympus), an EMCCD camera (iXion887; Andor Technology, pixel size = 189 nm), a pair of xy Galvo mirrors that are capable of switching from a TIRF light path to wide-field point-scanning bleaching illumination and is controlled with in-house C++ control software (developed by V. Polejaev, Yale University). Cells were imaged for 100 frames, photobleached for 2 s, and imaged by TIRFM again for 1500–2000 frames at a 6 frames per s frequency to detect fusion events for a total of 3 to 5 min. The 488 nm laser was adjusted to 50–60% of the power ($\sim 200 \mu\text{W}$ measured at the objective with a S170C microscope slide power sensor from Thorlabs). Detection and classification of fusion events was performed as described previously^{43, 44}. Image analysis and enhancement were carried out with ImageJ.

To image endocytosis of ecto-Halo $\beta 1$ in live cells, cells were labeled with 250 nM Alexa488 Halo ligand for 5 min, washed twice with medium at RT, and imaged live at 37 °C with a TIRFM microscope and HILO illumination. Images of 5 cells were acquired every 30 s for a total of 40 min. Surface fluorescence was then quenched with $5 \mu\text{g ml}^{-1}$ anti-Alexa488 antibody (Life technologies A11094) and cells were imaged for an additional 10 min. For co-localization with transferrin and the endosomal marker EEA1, Alexa488 Halo-labeled cells were incubated with $5 \mu\text{g ml}^{-1}$ Alexa568-transferrin (Tf568, Life technologies T23365) for 30 min in medium at 37 °C, fixed and stained for EEA1 (Cell signaling 3288T) by immunofluorescence as described above, and imaged by Wide-field illumination microscopy on an OMX microscope and deconvolution.

To label surface and internal pools of ecto-Halo $\beta 1$ integrins, cells plated in FN-coated MatTek dishes were labeled sequentially with 250 nM HaloTag Alexa Fluor 488 (Promega) and 250 nM Halo-reactive SiR647-chloroalkane (SiR647-CA, gift from Promega) diluted in imaging medium for 15–30 min each. Cells were

washed three times with imaging medium between and after labeling. The dynamics of sequentially labeled ecto-Halo $\beta 1$ integrins at FA were monitored by TIRFM for 1 h in live cells at 37 °C or on cells fixed 0 or 1 h after labeling.

For 3D imaging, sequentially labeled ecto-Halo $\beta 1$ integrin expressing cells plated on FN-coated MatTek dishes in imaging medium were imaged by confocal microscopy. We used a Yokogawa-type SDCM (Perkin-Elmer) mounted on an inverted microscope base (IX-71, Olympus) equipped with a 1×1 Kb electron-multiplying charge-coupled device camera (Hamamatsu Photonics), a temperature-controlled stage set (custom built), via a 60×1.4 NA oil objective lens with a pixel size of 143 nm using solid-state lasers: 488-, 640-nm (Melles Griot) with a 500 nm z-interval to image 8–10 μm of the cell volume. Acquisition and image analysis were performed using Volocity software (Perkin-Elmer).

Spatial image analysis and modeling. To test whether fusion events occur at or near FAs, we computed the shortest distance from each fusion event to a FA, using a custom script written in MATLAB (Mathworks, Natick, MA, USA). Namely, this computation used the coordinates of each fusion event (561 fusion events from 5 cells; i.e., ~ 46 –147 fusion events per cell) and corresponding binary masks identifying the position of FAs; the latter were generated using binary thresholding of the integrin channel prior to TIRFM photobleaching. For comparison, we simulated the same number of fusion events per cell (for each cell imaged) with random coordinates within the cell footprint, using Monte Carlo simulations (MATLAB plugin) for complete spatial randomness, and computed the shortest distance from these coordinates to FAs. This computation relied on binary masks identifying FAs (described above) while simulated coordinates of “fusion events” were randomly distributed within a manually defined binary mask identifying the cell. For each cell, this simulation was executed at least 100 times, yielding an average distance between randomly distributed coordinates and FAs. The real and synthetic data of each cell were plotted and compared by probability distribution functions.

Data availability. All relevant data and MATLAB scripts are available from the authors upon request.

Received: 12 October 2016 Accepted: 16 July 2017

Published online: 18 September 2017

References

- Iwamoto, D. V. & Calderwood, D. A. Regulation of integrin-mediated adhesions. *Curr. Opin. Cell Biol.* **36**, 41–47 (2015).
- Morse, E. M., Brahme, N. N. & Calderwood, D. A. Integrin cytoplasmic tail interactions. *Biochemistry* **53**, 810–820 (2014).
- Campbell, I. D. & Humphries, M. J. Integrin structure, activation, and interactions. *Cold Spring Harb. Perspect. Biol.* **3**, pii:a004994, doi:10.1101/cshperspect.a004994 (2011).
- De Franceschi, N., Hamidi, H., Alanko, J., Sahgal, P. & Ivaska, J. Integrin traffic—the update. *J. Cell Sci.* **128**, 839–852 (2015).
- Margadant, C., Monsuur, H. N., Norman, J. C. & Sonnenberg, A. Mechanisms of integrin activation and trafficking. *Curr. Opin. Cell Biol.* **23**, 607–614 (2011).
- Zhu, J., Zhu, J. & Springer, T. A. Complete integrin headpiece opening in eight steps. *J. Cell Biol.* **201**, 1053–1068 (2013).
- Fu, G., Wang, W. & Luo, B. H. Overview: structural biology of integrins. *Methods Mol. Biol.* **757**, 81–99 (2012).
- Shattil, S. J., Kim, C. & Ginsberg, M. H. The final steps of integrin activation: the end game. *Nat. Rev. Mol. Cell Biol.* **11**, 288–300 (2010).
- Calderwood, D. A., Campbell, I. D. & Critchley, D. R. Talin and kindlins: partners in integrin-mediated adhesion. *Nat. Rev. Mol. Cell Biol.* **14**, 503–517 (2013).
- Bridgewater, R. E., Norman, J. C. & Caswell, P. T. Integrin trafficking at a glance. *J. Cell Sci.* **125**, 3695–3701 (2012).
- Dozynkiewicz, M. A. et al. Rab25 and CLIC3 collaborate to promote integrin recycling from late endosomes/lysosomes and drive cancer progression. *Dev. Cell* **22**, 131–145 (2012).
- Muller, P. A. et al. Mutant p53 drives invasion by promoting integrin recycling. *Cell* **139**, 1327–1341 (2009).
- Rainero, E. & Norman, J. C. Late endosomal and lysosomal trafficking during integrin-mediated cell migration and invasion: cell matrix receptors are trafficked through the late endosomal pathway in a way that dictates how cells migrate. *Bioessays* **35**, 523–532 (2013).
- Bouvard, D., Pouwels, J., De Franceschi, N. & Ivaska, J. Integrin inactivators: balancing cellular functions in vitro and in vivo. *Nat. Rev. Mol. Cell Biol.* **14**, 430–442 (2013).
- De Franceschi, N. et al. Selective integrin endocytosis is driven by interactions between the integrin alpha-chain and AP2. *Nat. Struct. Mol. Biol.* **23**, 172–179 (2016).

16. Nader, G. P., Ezratty, E. J. & Gundersen, G. G. FAK, talin and PIPKIgamma regulate endocytosed integrin activation to polarize focal adhesion assembly. *Nat. Cell Biol.* **18**, 491–503 (2016).
17. Wang, Y. et al. Formin-like 2 promotes beta1-integrin trafficking and invasive motility downstream of PKCalpha. *Dev. Cell* **34**, 475–483 (2015).
18. Rainero, E. et al. Ligand-occupied integrin internalization links nutrient signaling to invasive migration. *Cell Rep.* **10**, 398–413 (2015).
19. Wehrle-Haller, B. Analysis of integrin dynamics by fluorescence recovery after photobleaching. *Methods Mol. Biol.* **370**, 173–202 (2007).
20. Laukaitis, C. M., Webb, D. J., Donais, K. & Horwitz, A. F. Differential dynamics of alpha 5 integrin, Paxillin, and alpha-actinin during formation and disassembly of adhesions in migrating cells. *J. Cell Biol.* **153**, 1427–1440 (2001).
21. Parsons, M., Messent, A. J., Humphries, J. D., Deakin, N. O. & Humphries, M. J. Quantification of integrin receptor agonism by fluorescence lifetime imaging. *J. Cell Sci.* **121**, 265–271 (2008).
22. Plancon, S., Morel-Kopp, M. C., Schaffner-Reckinger, E., Chen, P. & Kieffer, N. Green fluorescent protein (GFP) tagged to the cytoplasmic tail of alphaIIb or beta3 allows the expression of a fully functional integrin alphaIIb(beta3): effect of beta3GFP on alphaIIb(beta3) ligand binding. *Biochem. J.* **357**, 529–536 (2001).
23. Arnaout, M. A., Goodman, S. L. & Xiong, J. P. Structure and mechanics of integrin-based cell adhesion. *Curr. Opin. Cell Biol.* **19**, 495–507 (2007).
24. Los, G. V. et al. HaloTag: a novel protein labeling technology for cell imaging and protein analysis. *ACS Chem. Biol.* **3**, 373–382 (2008).
25. Nagae, M. et al. Crystal structure of alpha5beta1 integrin ectodomain: atomic details of the fibronectin receptor. *J. Cell Biol.* **197**, 131–140 (2012).
26. Xiong, J. P. et al. Crystal structure of the extracellular segment of integrin alphaVbeta3. *Science* **294**, 339–345 (2001).
27. Xiong, J. P. et al. Crystal structure of the extracellular segment of integrin alphaVbeta3 in complex with an Arg-Gly-Asp ligand. *Science* **296**, 151–155 (2002).
28. Xiong, J. P. et al. Crystal structure of the complete integrin alphaVbeta3 ectodomain plus an alpha/beta transmembrane fragment. *J. Cell Biol.* **186**, 589–600 (2009).
29. Dong, X. et al. alpha(V)beta(3) integrin crystal structures and their functional implications. *Biochemistry* **51**, 8814–8828 (2012).
30. Xiao, T., Takagi, J., Coller, B. S., Wang, J. H. & Springer, T. A. Structural basis for allostery in integrins and binding to fibrinogen-mimetic therapeutics. *Nature* **432**, 59–67 (2004).
31. Springer, T. A., Zhu, J. & Xiao, T. Structural basis for distinctive recognition of fibrinogen gammaC peptide by the platelet integrin alphaIIb beta3. *J. Cell Biol.* **182**, 791–800 (2008).
32. Zhu, J. et al. Structure of a complete integrin ectodomain in a physiologic resting state and activation and deactivation by applied forces. *Mol. Cell* **32**, 849–861 (2008).
33. Zhu, J. et al. Structure-guided design of a high-affinity platelet integrin alphaIIb beta3 receptor antagonist that disrupts Mg(2)(+) binding to the MIDAS. *Sci. Transl. Med.* **4**, 125ra132 (2012).
34. Zhu, J. et al. Closed headpiece of integrin alphaIIb beta3 and its complex with an alphaIIb beta3-specific antagonist that does not induce opening. *Blood* **116**, 5050–5059 (2010).
35. Xie, C. et al. Structure of an integrin with an alphaI domain, complement receptor type 4. *EMBO J.* **29**, 666–679 (2010).
36. Simpson, M. A. et al. Direct interactions with the integrin beta1 cytoplasmic tail activate the Abl2/Arg kinase. *J. Biol. Chem.* **290**, 8360–8372 (2015).
37. Bazzoni, G., Shih, D.-T., Buck, C. A. & Hemler, M. E. MAb 9EG7 defines a novel beta1 integrin epitope induced by soluble ligand and manganese, but inhibited by calcium. *J. Biol. Chem.* **270**, 25570–25577 (1995).
38. Schiller, H. B. et al. beta1- and alphav-class integrins cooperate to regulate myosin II during rigidity sensing of fibronectin-based microenvironments. *Nat. Cell Biol.* **15**, 625–636 (2013).
39. Werb, Z., Tremble, P. M., Behrendtsen, O., Crowley, E. & Damsky, C. H. Signal transduction through the fibronectin receptor induces collagenase and stromelysin gene expression. *J. Cell Biol.* **109**, 877–889 (1989).
40. Bouaouina, M., Harburger, D. S. & Calderwood, D. A. Talin and signaling through integrins. *Methods Mol. Biol.* **757**, 325–347 (2012).
41. Luque, A. et al. Activated conformations of very late activation integrins detected by a group of antibodies (HUTS) specific for a novel regulatory region (355–425) of the common beta 1 chain. *J. Biol. Chem.* **271**, 11067–11075 (1996).
42. Miesenböck, G., De Angelis, D. & Rothman, J. Visualizing secretion and synaptic transmission with pH-sensitive green fluorescent proteins. *Nature* **394**, 192–195 (1998).
43. Xu, Y. et al. Dual-mode of insulin action controls GLUT4 vesicle exocytosis. *J. Cell Biol.* **193**, 643–653 (2011).
44. Rivera-Molina, F. & Toomre, D. Live-cell imaging of exocyst links its spatiotemporal dynamics to various stages of vesicle fusion. *J. Cell Biol.* **201**, 673–680 (2013).
45. Sebastian, R. et al. Spatio-temporal analysis of constitutive exocytosis in epithelial cells. *IEEE/ACM Trans. Comput. Biol. Bioinform.* **3**, 17–32 (2006).
46. Toomre, D., Steyer, J. A., Keller, P., Almers, W. & Simons, K. Fusion of constitutive membrane traffic with the cell surface observed by evanescent wave microscopy. *J. Cell Biol.* **149**, 33–40 (2000).
47. Carman, C. V. Overview: imaging in the study of integrins. *Methods Mol. Biol.* **757**, 159–189 (2012).
48. Verschueren, H. Interference reflection microscopy in cell biology: methodology and applications. *J. Cell Sci.* **75**, 279–301 (1985).
49. Thapa, N. et al. Phosphoinositide signaling regulates the exocyst complex and polarized integrin trafficking in directionally migrating cells. *Dev. Cell* **22**, 116–130 (2012).
50. Bottanelli, F. et al. Two-colour live-cell nanoscale imaging of intracellular targets. *Nat. Commun.* **7**, 10778 (2016).
51. Los, G. V. & Wood, K. The HaloTag: a novel technology for cell imaging and protein analysis. *Methods Mol. Biol.* **356**, 195–208 (2007).
52. Tokunaga, M., Imamoto, N. & Sakata-Sogawa, K. Highly inclined thin illumination enables clear single-molecule imaging in cells. *Nat. Methods* **5**, 159–161 (2008).
53. Arjonen, A., Alanko, J., Veltel, S. & Ivaska, J. Distinct recycling of active and inactive beta1 integrins. *Traffic* **13**, 610–625 (2012).
54. Kucic, I., Rivera-Molina, F. & Toomre, D. The IN/OUT assay: a new tool to study ciliogenesis. *Cilia* **5**, 23 (2016).
55. Humphries, M. J. Cell adhesion assays. *Methods Mol. Biol.* **522**, 203–210 (2009).
56. Roberts, M., Barry, S., Woods, A., van der Sluijs, P. & Norman, J. PDGF-regulated rab4-dependent recycling of alphavbeta3 integrin from early endosomes is necessary for cell adhesion and spreading. *Curr. Biol.* **11**, 1392–1402 (2001).
57. Gabriel, L., Stevens, Z. & Melikian, H. Measuring plasma membrane protein endocytic rates by reversible biotinylation. *J. Vis. Exp.* <http://dx.doi.org/10.3791/1669> (2009).

Acknowledgements

This work was supported by grants from the National Institutes of Health (R01GM068600 and R01NS085078 to D.A.C.; R01GM098498 to D.T., and T32GM007324, and T32GM007223), the American Cancer Society (RSG-12-053-01, D.A.C.), the Wellcome Trust Foundation (D.T.), and the American Heart Association (15PRE25700119, D.V.I.). We thank Promega for providing the Halo-reactive SiR647-CA Ligand, and Giulia Villari and Elizabeth Morse for help with initial integrin cloning.

Author contributions

D.A.C., D.T., C.H.-C. and F.R.-M. conceived and designed the research and prepared the manuscript. C.H.-C. and F.R.-M. performed most experiments and data analyses. D.V.I. provided key reagents and helped with flow cytometry integrin activation assays. E.B.K. provided custom algorithm and helped with statistical analysis of spatial distribution of fusion events.

Additional information

Supplementary Information accompanies this paper at doi:10.1038/s41467-017-00646-w.

Competing interests: The authors declare no competing financial interests.

Reprints and permission information is available online at <http://npg.nature.com/reprintsandpermissions/>

Publisher's note: Springer Nature remains neutral with regard to jurisdictional claims in published maps and institutional affiliations.



Open Access This article is licensed under a Creative Commons Attribution 4.0 International License, which permits use, sharing, adaptation, distribution and reproduction in any medium or format, as long as you give appropriate credit to the original author(s) and the source, provide a link to the Creative Commons license, and indicate if changes were made. The images or other third party material in this article are included in the article's Creative Commons license, unless indicated otherwise in a credit line to the material. If material is not included in the article's Creative Commons license and your intended use is not permitted by statutory regulation or exceeds the permitted use, you will need to obtain permission directly from the copyright holder. To view a copy of this license, visit <http://creativecommons.org/licenses/by/4.0/>.

© The Author(s) 2017